Journal of Materials Chemistry A

ROYAL SOCIETY OF CHEMISTRY

PAPER

View Article Online
View Journal | View Issue

Cite this: J. Mater. Chem. A, 2024, 12, 6693

Unraveling the photocatalytic potential of transition metal sulfide and selenide monolayers for overall water splitting and photo-corrosion inhibition†

Shafiq Ur Rehman,[ab] Junwei Wang,[ab] Guixuan Wu,[c] Sajjad Ali,[d] Jian Xian *[ab] and Nasir Mahmood *[e]

Photocatalytic water splitting is a promising route to alleviate energy crises and provide clean renewable energy. However, finding the right materials for photocatalytic water splitting is challenging owing to its multilevel complexity. Herein, transition metal sulfide and selenide (TMSS) monolayers were screened to find the best possible monolayers for overall water splitting. Properties such as suitable band edges, oxidation and reduction potential, catalytic activities and solar to hydrogen (STH) efficiency were considered. Among various TMSS monolayers, MoS_2, WS_2, $PtSe_2$, $PdSe_2$, and $NiSe_2$ have suitable conduction and valence band edges to trigger the oxygen evolution reaction (OER) and hydrogen evolution reaction (HER) simultaneously in acidic media. Moreover, the MoS_2, $PtSe_2$, $PdSe_2$ and $NiSe_2$ monolayers can effectively resist oxidative and reductive photo-corrosion in acidic and WS_2 monolayers in neutral environments during water splitting. All monolayers have robust catalytic activities in the predicted electrolytes with HER overpotential near zero, and OERs are 0.53, 1.01 and 0.99 V for $PtSe_2$, $PdSe_2$ and $NiSe_2$ monolayers, respectively. The STH efficiencies were also found to be high for MoS_2 (10.4%), $PtSe_2$ (22.2%), $PdSe_2$ (19.6%), $NiSe_2$ (20.1%) in acidic medium and WS_2 (11.1%) in neutral medium. The predicted monolayers show promise for practical application as bifunctional photocatalysts in acidic and neutral environments.

Received 17th November 2023
Accepted 5th February 2024

DOI: 10.1039/d3ta07106e

rsc.li/materials-a

1. Introduction

The utilization of photocatalytic water splitting is a promising approach for generating sustainable and clean hydrogen fuels.[1] It has the potential to revolutionize energy consumption patterns and reduce the environmental impacts of fossil fuel usage. Since the discovery of TiO_2 photocatalyst, various oxide-based photocatalysts have been developed for water splitting, CO_2 reduction, organic pollutant degradation and sustainable energy production.[2–9] Owing to their inherent stability in water and other electrolyte solutions, oxide materials are still under research and are garnering global interest among researchers.[10–12] However, oxide photocatalysts have large energy gaps (4–5) eV, low hydrogen conversion efficiency (<1%), and a high recombination rate of photoexcited electrons and holes, further reducing the catalytic activity and output products. Compared with traditional oxide materials, two-dimensional (2D) transition metal sulfide and selenide (TMSS) monolayers have several advantages for photocatalytic applications. They have a large surface area, tuneable energy gaps, visible light absorption, high stability and low exciton binding energies.[13–19] Their layer-dependent electronic properties and optical absorption make TMSS monolayers more attractive to solar water splitting and a suitable alternative to oxide-based photocatalysis.

Several studies have reported TMSS monolayer photocatalysts for HER and CO_2 reduction, which is a new green route to solving energy crises.[13,20–27] Among them, the 2H-MoS_2 and 1T-MoS_2 monolayers with Pt as co-catalysts have been studied for HER in acidic media.[26] The HER performance of 2H-MoS_2 and 2H-$MoTe_2$ monolayers has been upgraded by tunning the phase boundaries and basal plane.[27,28] The atomistic insights into the 2H phase WSe_2 monolayer photocatalyst have uncovered its potential for HER and CO_2 reduction.[29] 1T-MoS_2 monolayer has shown a comparatively high hydrogen production rate (600 μmol h^{-1}) compared to precious noble metals

[a]Yangtze Delta Region Institute (Huzhou), University of Electronic Science and Technology of China, Huzhou 313001, China. E-mail: jianxian@uestc.edu.cn
[b]School of Materials and Energy, University of Electronic Science and Technology of China, Chengdu, 611731, China
[c]State Key Laboratory of Coal Conversion, Institute of Coal Chemistry, Chinese Academy of Sciences, Taiyuan, 030001, China
[d]Energy, Water, and Environment Lab, College of Humanities and Sciences, Prince Sultan University, Riyadh 11586, Saudi Arabia
[e]School of Science, RMIT University, 124 La Trobe Street, 3001 Melbourne, Victoria, Australia. E-mail: nasir.mahmood@rmit.edu.au

† Electronic supplementary information (ESI) available. See DOI: https://doi.org/10.1039/d3ta07106e

such as Pt (450 μmol h^{-1}), Pd (230 μmol h^{-1}) and Au (70 μmol h^{-1}).[13] TMSS monolayers in different phases have shown stability for HER against photo-corrosion in aqueous solution.[23,29–32] To date, TMSS monolayer catalysts have predominantly shown their potential for HER cathodic reactions either in acidic or alkaline media. However, these catalysts may suffer from photo-degradation and photo-corrosion when HER and OER electrodes are paired in the same electrolyte towards overall water splitting (OWS). The photo-degradation is caused by the unsuitable band edges of the materials for OWS and photo-corrosion owing to the unfavourable pH environment for both HER and OER simultaneously. This may cause poor catalytic activities and reduce the efficiency of the photocatalyst. The formation of a bi-functional photocatalyst, which can trigger both HER and OER simultaneously in a single electrolyte, has great potential in the application of OWS. Therefore, it is necessary to study the thermodynamic suitability of conduction and valence band edges of TMSS monolayers towards OWS. Second, the calculation of oxidation and reduction potentials with respect to (w.r.t.) the normal hydrogen electrode (NHE) of the monolayers is crucial owing to their aqueous stability. When both conditions are satisfied, the photocatalyst resists photo-decomposition and photo-corrosion. For practical applications, it is also important to address the pH effect of electrolytes on the band edges and thermodynamic potentials of monolayers and to study catalytic activities and STH efficiency.

As there are many TMSS monolayers, it is difficult for experimentalists to pick up the right candidate with suitable band edges for OWS as well as show resistance against photo-corrosion in aqueous media. Density functional theory (DFT) is a powerful quantum mechanical tool that can quickly identify materials with suitable band edges and a favourable pH environment for photocatalytic OWS. In the present work, we performed DFT calculations and screened 500 TMSS monolayers with suitable conduction and valence band edges for water reduction and oxidation, respectively. Among them, only seven (7) TMSS monolayers are identified with thermodynamically stable band edges towards OWS. The G_0W_0 calculated band edges show that only CrS_2, MoS_2, $MoSe_2$, WS_2 and $PtSe_2$ monolayers can trigger HER and OER simultaneously in acidic media. The conduction and valence band edges of these monolayers are favourable for water reduction and oxidation in an acidic environment, respectively. These materials have high exciton potentials that can split H_2O molecules into H_2 and O_2 and can show resistance to photo-decomposition caused by them. Furthermore, the thermodynamic oxidation and reduction potentials show that MoS_2, WS_2, $PtSe_2$, $PdSe_2$ and $NiSe_2$ monolayers are strongly resistant to oxidative and reductive photo-corrosion at pH 4.6–8, 6.1–6.7, 0–5.9, 0–3.8 and 3–5.2, respectively. We predict that these monolayers can be effectively utilized in OWS in their respective pH environments. The band edges and thermodynamic potentials of the monolayers can be adjusted by tunning the pH level of the electrolyte. The monolayers exhibit high STH efficiencies and excellent HER and OER activities with low overpotentials in the predicted favourable pH environment.

2. Computational details

Initial computations were conducted by employing the Vienna *Ab initio* Simulation Package (VASP), with the generalized gradient approximation (GGA-PBE) to account for electron exchange correlation effects.[33,34] A plane wave cut-off energy of 450 eV was selected for the energy calculations and 400 eV for G_0W_0 calculations. The relaxation of a $3 \times 3 \times 1$ supercell for the specified TMSS monolayers was carried out using a force criterion of 0.01 eV $Å^{-1}$. In this study, the (s_1, d_9) states were designated as valence states for transition metals, whereas the valence states for both sulphur (S) and selenium (Se) atoms were considered as (s_2, p_4). A 15 Å vacuum was implemented along the *c*-direction within the unit cell of each monolayer to mitigate self-interactions. The G_0W_0 method was employed to accurately determine the band edges of the identified materials. For both PBE and G_0W_0 calculations, a *k*-mesh of $13 \times 13 \times 1$ was utilized during the structural relaxation.[35] The refinement of geometries in TMSS monolayers considered the van der Waals (vdW) energy correction term, employing the DFT-D3 approach (Grimme's semi-empirical corrections).[36]

Notably, the heavy transition elements exhibit pronounced relativistic effects, particularly due to spin–orbit coupling. Consequently, specialized spin–orbit and relativistic pseudopotentials were incorporated into the calculations to account for these effects. Additionally, the calculations considered the solvation effect for a comprehensive assessment.[37] The correction for gas phase molecules was calculated with the accurate molecular thermodynamic model for entropy and free energy ($G = H - TS$) as implemented in quantum espresso code,[38] where G is the free energy, H is enthalpy, T is temperature and S is the entropy in gas phases. The contribution of solids was calculated according to ($F = U - TS$), with phonon calculation in phonopy code,[39] where F is the free energy contributed by vibration for solids, U is the internal energy and S is entropy contributed by vibrations.

3. Results and discussion

3.1 Thermodynamic stability and pH effects

First, a rigorous screening process was performed on five hundred (500) TMSS monolayers in two well-known phases, *i.e.*, octahedral (1T) and tetragonal prismatic (2H). This comprehensive search was conducted across the C2DB database with the data meticulously validated against existing literature.[40–44] For a photocatalyst to split the water molecule into O_2 and H_2, it is necessary that the conduction band edge (E_{CBM}) and valence band edge (E_{VBM}) w.r.t. vacuum levels are higher and lower than the standard potentials of hydrogen reduction $E(H^+/H_2) = -4.44$ eV and oxygen reduction $E(O_2/H_2O) = -5.67$ eV, respectively. These are the conditions for thermodynamic favourability of the reduction, and oxidation half reactions are presented in eqn (1) and (2):

$$E_{CBM} > E(H^+/H_2), \quad (1)$$

$$E_{VBM} < E(O_2/H_2O). \quad (2)$$

By employing the two conditions, seven (7) TMSS monolayers are identified with suitable band edge positions w.r.t. water redox potentials. The band alignment diagram of seven monolayers with suitable band edges for water splitting is illustrated in Fig. S1 of the ESI.† The top and side views of the optimized structures of the seven TMSS monolayers with suitable band edges for OWS are shown in Fig. S2.† To enable the process of OWS, the chosen photocatalyst must feature a precise band alignment that aligns with the redox potentials of water. Simultaneously, the photoexcited electrons and holes should offer ample driving force to effectively initiate HER and OER, respectively. Therefore, we calculated the accurate CBM and VBM of the promising TMSS monolayers using G_0W_0 method, as shown in Fig. 1(a). G_0W_0 method is a highly reliable method for the calculation of band edges of the materials, and the energy gaps based on this method can be directly compared with the experimental energy gaps.[42–44] The alignment of the conduction band and valence band edges w.r.t. vacuum level is achieved through a meticulous matching of planar-averaged electrostatic potential in the layer with the corresponding potential in the vacuum region. The planar-averaged electrostatic potential is calculated with G_0W_0, as shown in Fig. S3 in the ESI.†

Fig. 1(a) shows that the CBM (black bars) of selected TMSS monolayers (CrS_2, MoS_2, $MoSe_2$, WS_2, $NiSe_2$, $PdSe_2$, $PtSe_2$) is higher than the standard potential of hydrogen (−4.44 eV) at pH = 0. The first condition of thermodynamic stability is satisfied by these monolayers, and the electrons in their CBM have enough potential to split the water molecules and trigger the HER process. For the OER process, the monolayers CrS_2, MoS_2, $MoSe_2$, WS_2 and $PtSe_2$ exhibit suitable VBM at pH = 0, while $NiSe_2$ and $PdSe_2$ do not have suitable VBM to trigger the process. The CrS_2, MoS_2, $MoSe_2$, WS_2 and $PtSe_2$ monolayers can trigger HER and OER simultaneously, and these could be promising materials for OWS. The electron potential (U_e) concerning hydrogen reduction and the hole potential (U_h) governing water oxidation exemplify the redox capabilities of photogenerated carriers. Consequently, U_e and U_h served as pivotal criteria for assessing photocatalyst performance in the water splitting process. U_e for the HER is defined as the difference between the CBM and the redox potential of hydrogen, while U_h represents the difference between the VBM and the redox potential of oxygen. The calculated values of U_e for MoS_2, WS_2, $MoSe_2$, CrS_2, $PtSe_2$, $PdSe_2$ and $NiSe_2$ are 1.34, 1.18, 1.7, 1.0, 0.79, 0.60 and 0.3 (unit, V), respectively. The calculated photogenerated hole potentials (U_h) are 1.31, 1.32, 0.64, 1.36, 1.4, 0.76 and 0.48 (unit, V) for MoS_2, WS_2, $MoSe_2$, CrS_2, $PtSe_2$, $PdSe_2$ and $NiSe_2$ monolayers, respectively. The exciton potentials of selected TMSS monolayers are much higher than the reported work,[45–48] indicating high redox abilities for HER and OER. The CBM and VBM edges of the selected TMSS monolayers exhibit a pH-dependent shift. Specifically, for HER, the CBM edge varies with pH based on the formula −4.44 + pH × 0.059 eV,

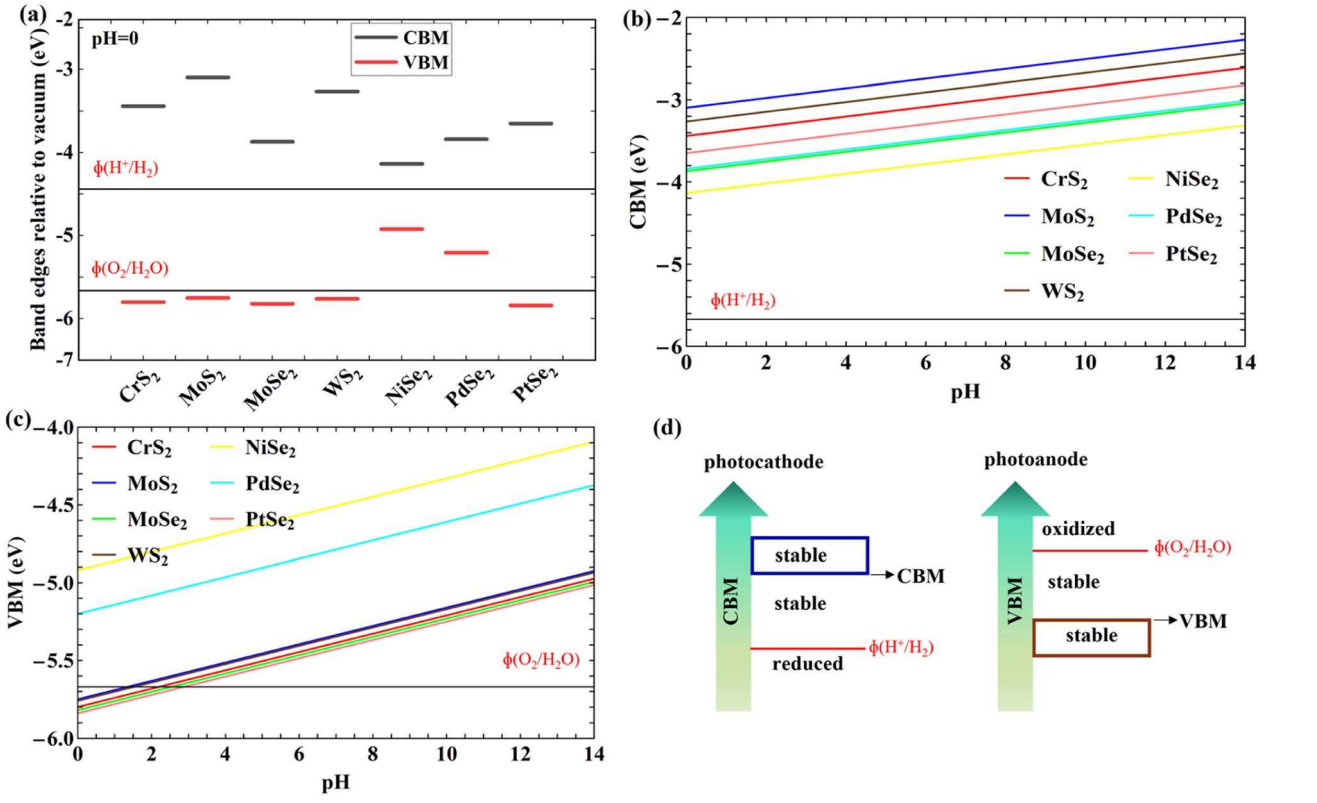

Fig. 1 (a) G_0W_0 calculated CBM (black bars) and VBM (red bars) w.r.t. vacuum level for TMSS monolayers at pH = 0. (b) pH dependency of CBM, and (c) pH dependency of VBM, where the horizontal straight lines represent the standard redox potentials of HER (−4.44 eV) and OER (−5.67 eV). (d) Stability changes in the photocathode as CBM moves down of $\phi(H^+/H_2)$ and for photoanode as VBM shifts up of $\phi(O_2/H_2O)$.

emphasizing a dynamic response to the pH of the environment. Conversely, for OER, the VBM edge shifts with pH according to the formula $-5.66 + \text{pH} \times 0.059$ eV.[49]

Fig. 1(b) shows a linear increase in the CBM with an increase in the pH value for monolayers, and CBM modulation is above the reduction potential (−4.44 eV) of hydrogen. This suggests that the selected monolayers are suitable for HER in acidic, neutral and alkaline environments, and TMSS monolayers are well known for their stability and working for hydrogen evolution in acidic and alkaline solutions.[30,49–51] As shown in Fig. 1(c), the VBM of the monolayers CrS_2, MoS_2, $MoSe_2$, WS_2 and $PtSe_2$ is suitable for OER in different pH ranges, such as (0–2), (0–2.2), (0–2.5), (0–1.6) and (0–3), respectively. The VBM of $NiSe_2$ and $PdSe_2$ monolayers is not straddled with the oxidation potential for OER throughout the pH range, as shown in Fig. 1(c). When the pH value increases, the VBM of monolayers CrS_2, MoS_2, $MoSe_2$, WS_2 and $PtSe_2$ becomes unstable towards water oxidation. This is because the VBM of the monolayers shifts above the oxidation potential (−5.67 eV) of water. However, CrS_2, MoS_2, $MoSe_2$, WS_2 and $PtSe_2$ monolayers are thermodynamically stable band edges in acidic environment, and their thermodynamics can be controlled by tuning the pH of electrolytes. The selected monolayers can be practically applied as anodic (OER) and cathodic (HER) simultaneously in an acidic environment. The monolayers resist photo-decomposition as long as their CBM and VBM edges satisfy conditions (1) and (2), respectively. Fig. 1(d) shows a general illustration of the thermodynamic stability change in the photocathode as CBM moves down of standard reduction potential ($\phi(H^+/H_2)$) and for photoanode as VBM shifts up of oxidation potential ($\phi(O_2/H_2O)$) of water.

3.2 Aqueous stability and photo-corrosion inhibition

In addition to the suitable band edges of TMSS monolayers for OWS, the important and necessary conditions are their stability in an aqueous environment and photo-corrosion inhibition. The assessment of aqueous stability and photo-corrosion inhibition followed a model designed for oxide semiconductors in aqueous solutions.[52] The model facilitates the calculation of thermodynamic oxidation and reduction potentials for the materials through eqn (3) and (4), providing crucial insights into their overall performance under the following relevant conditions:

$$\phi^{red} = -\left[\frac{\Delta G}{eF}\right] + \phi(H^+/H_2), \quad (3)$$

$$\phi^{ox} = \left[\frac{\Delta G}{neF}\right] + \phi(H^+/H_2), \quad (4)$$

where ϕ^{ox} and ϕ^{red} represent the thermodynamic oxidation and reduction potentials, respectively; n is the number of electrons; F is the Faraday constant (96.5 kJ mol^{-1}); ΔG is the Gibbs free energy change; and $\phi(H^+/H_2)$ is the normal hydrogen electrode (NHE) potential at pH = 0. The stability conditions for photoanode is $\phi^{ox} > \phi(O_2/H_2O = 1.23\ V)$ and for the photocathode is $\phi^{red} < \phi(H^+/H_2 = 0\ V)$. The calculated ϕ^{red} and ϕ^{ox} for the selected TMSS monolayers are presented in Table S2.† The first column represents the monolayers, and the second column represents the oxidation and reduction reactions. In the oxidation and reduction reactions, the Gibbs free energy change ($\Delta ZPE - T\Delta S$), and total electronic energy change (ΔE) is given in the third and fourth columns of Table S2.† The calculated oxidation and reduction potentials of numerical values are given in the second to last column. The three values of oxidation and reduction potentials are taken at different pressure ranges (10^{-2}–10^{-4}) atm for the gas species involved in the reactions. We notice that the pressure has an insignificant effect on the oxidation and reduction potentials of the materials during the water splitting process.

The calculated reduction potential (red bars) and oxidation potential (blue bars) for MoS_2, WS_2, $MoSe_2$, CrS_2, $PtSe_2$, $PdSe_2$ and $NiSe_2$ monolayers are shown in Fig. 2(a), where the solid black lines are the standard water redox potentials for OER (1.23 V) and HER (0 V) at pH = 0. As shown in Fig. 2(a), the reduction potential of the promising TMSS monolayers is negative w.r.t. standard potential of HER at pH = 0. The TMSS monolayers satisfy the stability condition of a photocathode for water splitting, *i.e.*, $\phi^{red} < \phi(H^+/H_2 = 0\ V)$ and are thermodynamically stable for HER anodic reaction at pH = 0. This also indicates that TMSS monolayers possess a robust capability to withstand reductive photo-corrosion under extremely acidic conditions at pH = 0. For the oxidation case, only $PdSe_2$ and $PtSe_2$ monolayers have oxidation potential that straddled the standard potential of OER and satisfied the requirement of photoanode materials in half cell reaction at pH = 0, as shown in Fig. 2(a). Moreover, $PdSe_2$ and $PtSe_2$ monolayers can resist oxidative photo-corrosion at pH = 0. The monolayers MoS_2, WS_2, $MoSe_2$, CrS_2 and $NiSe_2$ oxidize and decompose in the electrolyte before triggering the OER reaction at pH = 0. This is because the oxidation potential of these monolayers is not straddled with the standard potential of OER (1.23 V) at pH = 0. However, the oxidation and reduction potentials can also be adjusted and controlled by the pH level of the electrolyte, as shown in Fig. 2(b and c). The reduction potentials of the TMSS monolayers linearly increase with an increase in the pH level of the electrolyte. TMSS monolayers become less stable as their reduction potential approaches the HER standard potential at pH = 0, as shown in Fig. 2(b). The oxidation potentials also increase with an increase in the pH level, and the TMSS monolayers become more stable towards the OER, as shown in Fig. 2(c). Monolayers $PdSe_2$ and $PtSe_2$ exhibit oxidation potential above the oxidation potential of water (1.23 V) throughout the pH range (0–14), which indicate that both monolayers are quite stable in acidic and alkaline environments and can strongly resist oxidative photo-corrosion. The stable pH range in which the reduction and oxidation potentials for MoS_2, WS_2, $MoSe_2$, CrS_2, $PtSe_2$, $PdSe_2$ and $NiSe_2$ monolayers can resist the reductive and oxidative photo-corrosion are shown in Table 1.

For OWS, the monolayers must have suitable reduction and oxidation potentials at a common pH that can straddle the redox potentials of HER and OER respectively. Therefore, we evaluated a common pH range and found that MoS_2, WS_2, $PtSe_2$, $PdSe_2$ and $NiSe_2$ monolayers are suitable for OWS in a common pH range, as shown in Table 1. The common pH

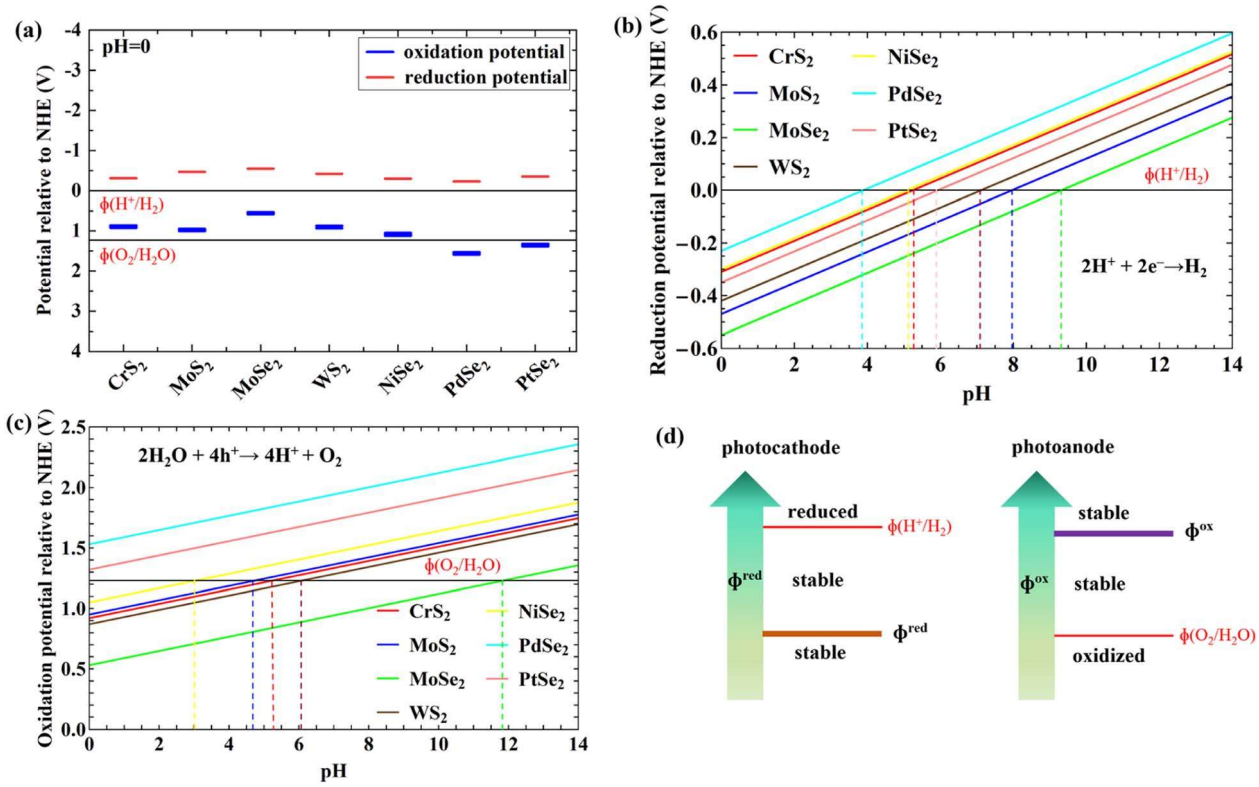

Fig. 2 (a) Reduction (red bars) and oxidation (blue bars) potentials relative to NHE of TMSS monolayers at pH = 0, (b) pH dependence of reduction potential, (c) pH dependence of oxidation potential and (d) stability changes in the photocathode as the reduction potential (ϕ^{red}) shifts above $\phi(H^+/H_2)$ and for photoanode as oxidation potential (ϕ^{ox}) shifts below $\phi(O_2/H_2O)$.

range for MoS_2, $PtSe_2$, $PdSe_2$ and $NiSe_2$ monolayers shows that they are stable in acidic media and WS_2 monolayer in neutral medium. Moreover, these chosen monolayers effectively withstand both reductive and oxidative photo-corrosion within their typical pH ranges. Monolayers CrS_2 and $MoSe_2$ lack a shared pH range for reduction and oxidation potentials, making them unsuitable for OWS and susceptible to photo-corrosion. As shown in Table 1, the selected TMSS monolayers are stable and resistant to photo-corrosion in acidic media in a specific shared pH range for OWS, and the stability of these monolayers in different phases and nanostructure formations has been confirmed in several experimental reports in acidic and alkaline solutions.[15,30,53–58] The MoS_2, $PtSe_2$, $PdSe_2$ and $NiSe_2$ monolayers hold promise as a bi-functional photocatalyst towards OWS in acidic media and WS_2 monolayer in neutral medium. A general illustration of the stability changes in the photocathode and photoanode with the change in the reduction and oxidation potentials is shown in Fig. 2(d). For a stable photocathode, the reduction potential must be lower than zero, and for a photoanode, the oxidation potential is above 1.23 V.

4. Photocatalytic activities

In the process of OWS, incident photons are absorbed by the photocatalyst, leading to the generation of electron–hole pairs. Electrons acted as reducing agents for H_2 production through a two-step process called HER half-cell reaction ($2H^+ + 2e^- \rightarrow H_2$), and holes acted as oxidizing agents responsible for the production of O_2 through the OER half-cell reaction ($2H_2O + 4h^+ \rightarrow 4H^+ + O_2$).[59] The OER anodic reaction is a challenging four-step process,

Table 1 Selected TMSS monolayers and their stable pH range for HER and OER, common pH for OWS, monolayers stable for OWS (✓), monolayers not stable for OWS (✗), STH efficiency (%) and OER overpotentials (V)

System	pH for HER	pH for OER	Common pH	pH for OWS	STH efficiency	OER overpotential
CrS_2	0–5.38	5.25–14		✗	—	—
MoS_2	0–8.0	4.6–14	4.6–8	✓	10.4	1.46
$MoSe_2$	0–8.0	11.8–14		✗	—	—
WS_2	0–7.1	6.1–14	6.1–7.1	✓	11.1	1.43
$NiSe_2$	0–5.2	3–14	3–5.2	✓	20.1	0.91
$PdSe_2$	0–3.8	0–14	0–3.8	✓	19.6	1.01
$PtSe_2$	0–5.9	0–14	0–5.9	✓	22.2	0.53

which requires four photo-holes to generate one oxygen molecule from two water molecules, as shown in the reactions below (5)–(9). In the first step of the OER process, a water molecule reacted with the photocatalyst in the presence of a hole and produced one hydrogen ion and an OH* intermediate. In the second step, the OH* intermediate reacted with a hole and transformed to the O* intermediate with the release of one hydrogen ion. In the third step, the O* intermediate reacted with a hole in the presence of a water molecule to generate an O–H–O* intermediate and release one hydrogen ion. In the last step, the O–H–O* intermediate reacted with the hole and give O_2^* and another hydrogen ion, but O_2^* is unstable and can immediately be desorbed from the photocatalyst surface as an O_2 molecule. The four-step process is presented in the following equations:

$$H_2O_{(l)} + * + h^+ \rightarrow OH^* + H^+ \quad (5)$$

$$OH^* + h^+ \rightarrow O^* + H^+ \quad (6)$$

$$O^* + H_2O_{(l)} + h^+ \rightarrow O\text{–}H\text{–}O^* + H^+ \quad (7)$$

$$O - H - O^* + h^+ \rightarrow O_2^* + H^+ \quad (8)$$

$$O_2^* + h^+ \rightarrow * + O_{2(g)}. \quad (9)$$

Meanwhile, the HER cathodic reaction is a two-step process given below in eqn (10) and (11).

$$* + H^+ + e^- \rightarrow H^* \quad (10)$$

$$* + H^+ + e^- \rightarrow H_{2(g)}, \quad (11)$$

where * represents the monolayers, such as MoS_2, WS_2, $PtSe_2$, $PdSe_2$, and $NiSe_2$, while OH*, O*, O–H–O*, O_2^* and H* are the intermediates, which are chemically very reactive with the surrounding environment. The Gibbs free energy differences, ΔG (eV) in eqn (12)–(18) of water redox reactions, are calculated according to the approach proposed by Nørskov.[60] The formula at pH = 0 is defined as $\Delta G = \Delta E + \Delta E_{zpe} - T\Delta S$, where ΔE is the adsorption energy difference, and ΔE_{zpe} and ΔS are the difference in zero-point energy and entropy difference between the adsorbed state and the gas phases, respectively. For each reaction of OER and HER, the free energy differences under the effect of an external potential bias are presented in the following equations:

$$\Delta G_1 = G_{OH^*} + G_{H^+} - G_{H_2O} - (*) - U_h \quad (12)$$

$$\Delta G_2 = G_{O^*} + G_{H^+} - G_{OH^*} - U_h \quad (13)$$

$$\Delta G_3 = G_{O\text{–}H\text{–}O^*} + G_{H^+} - G_{O^*} - G_{H_2O} - U_h \quad (14)$$

$$\Delta G_4 = G_{O_2^*} + G_{H^+} - G_{O\text{–}H\text{–}O^*} - U_h \quad (15)$$

$$\Delta G_5 = (*) + G_{O_2} - G_{O_2^*} - U_h \quad (16)$$

$$\Delta G_6 = G_{H^*} - (*) - G_{H^+} - U_e \quad (17)$$

$$\Delta G_7 = G_{H_2} - (H^*) - G_{H^+} - U_e. \quad (18)$$

The free energy (G_{H^+}) is replaced by $\frac{1}{2}G_{H_2}$ under standard conditions of pressure and temperature. Moreover, the catalytic performance is determined by the overpotential (η) for the reaction, which is defined by the maximum potential needed to downhill all the intermediate reaction steps. The theoretical overpotential (η) for OER in the four-step process can be calculated as $\eta_{OER} = \max[\Delta G_1, \Delta G_2, \Delta G_3, \Delta G_4, \Delta G_5]/e - 1.23$, where 1.23 V is the oxidation potential required for the oxidation of H_2O molecule into H_2 and O_2 under standard conditions of pressure and temperature; ΔG_1, ΔG_2, ΔG_3, ΔG_4 and ΔG_5 are the maximum change in free energy during the reactions and e is the electron charge. First, we studied the complicated water oxidation half reaction on the surfaces of promising monolayers following the four-hole reaction pathway, which is accompanied by the formation of adsorbed OH*, O*, O–H–O* and O_2^* intermediates. During the adsorption of OH*, O*, O–H–O* and O_2^* intermediates on the monolayers, we notice that the active species moved to the site of the chalcogen (S, Se) atoms because of their high electronegativity and then to the transition metals. The optimized intermediate-adsorbed structures of 3 × 3 × 1 supercell for 2H-MoS_2 and 1T-$PtSe_2$ monolayers are shown in Fig. S4 of ESI.† Similarly, the energy calculations of five intermediates were performed using the 3 × 3 × 1 supercell of 2H-WS_2, 1T-$PdSe_2$, 1T-$PtSe_2$ and 1T-$NiSe_2$ monolayers.

The calculated ΔG (eV) for MoS_2, WS_2, $PtSe_2$, $PdSe_2$ and $NiSe_2$ monolayers are shown in Fig. 3(a–e) with their corresponding pH values. We initially considered a situation without any external potential, *i.e.*, to simulate the condition in the absence of any light irradiation ($U_h = 0$). In this case, the energy landscape is non-spontaneous for all the monolayers. The ΔG value is very high at OH* and O–H–O* steps for MoS_2 and WS_2 monolayers, as shown in Fig. 3(a and b). The reason for the high energy barrier of these two steps is the low binding strength of OH* and O–H–O* species on the surface of monolayers. At hole potential zero, the calculated OER overpotentials for MoS_2 and WS_2 monolayers are 2.77 and 2.27 (unit, V), respectively. The overpotentials for OER in the presence of light are 1.46 and 1.34 (unit, V) for MoS_2 and WS_2 monolayers, respectively. The high overpotentials for OER on MoS_2 and WS_2 monolayers can be reduced when light is turned on. For 1T phase monolayers, such as $PdSe_2$, $NiSe_2$ and $PtSe_2$, the energy barrier at OH* and O–H–O* is comparatively low, as shown in Fig. 3(c–e). The calculated overpotentials for the OER at hole potential zero are 1.87, 1.7 and 0.53 (unit, V) for $NiSe_2$, $PdSe_2$ and $PtSe_2$ monolayers, respectively. When the hole potential was applied, then the OER reactions at the monolayer surfaces required relatively low energy at each intermediate step, as shown in the red energy landscape in Fig. 3(c–e). The overpotentials for OER in the absence of light are 0.91, 1.01 and 0.53 (unit, V) for $NiSe_2$, $PdSe_2$ and $PtSe_2$ monolayers, respectively. The low value of overpotentials for $NiSe_2$, $PdSe_2$ and $PtSe_2$ monolayers means that they could be the best candidates for OER. It is noteworthy that the ΔG (eV) for OER is pH dependent according to the Nernstian equation, so the overpotentials can be adjusted by tuning the pH value.[52]

The ΔG (eV) of HER for the 2H phase MoS_2 and WS_2 monolayers at pH = 4 and 6, respectively, are shown in Fig. 4(a). ΔG (eV) of HER for 1T phase $NiSe_2$, $PdSe_2$ and $PtSe_2$ monolayers at pH = 3 is shown in Fig. 4(b). MoS_2, WS_2, $PtSe_2$, $PdSe_2$ and

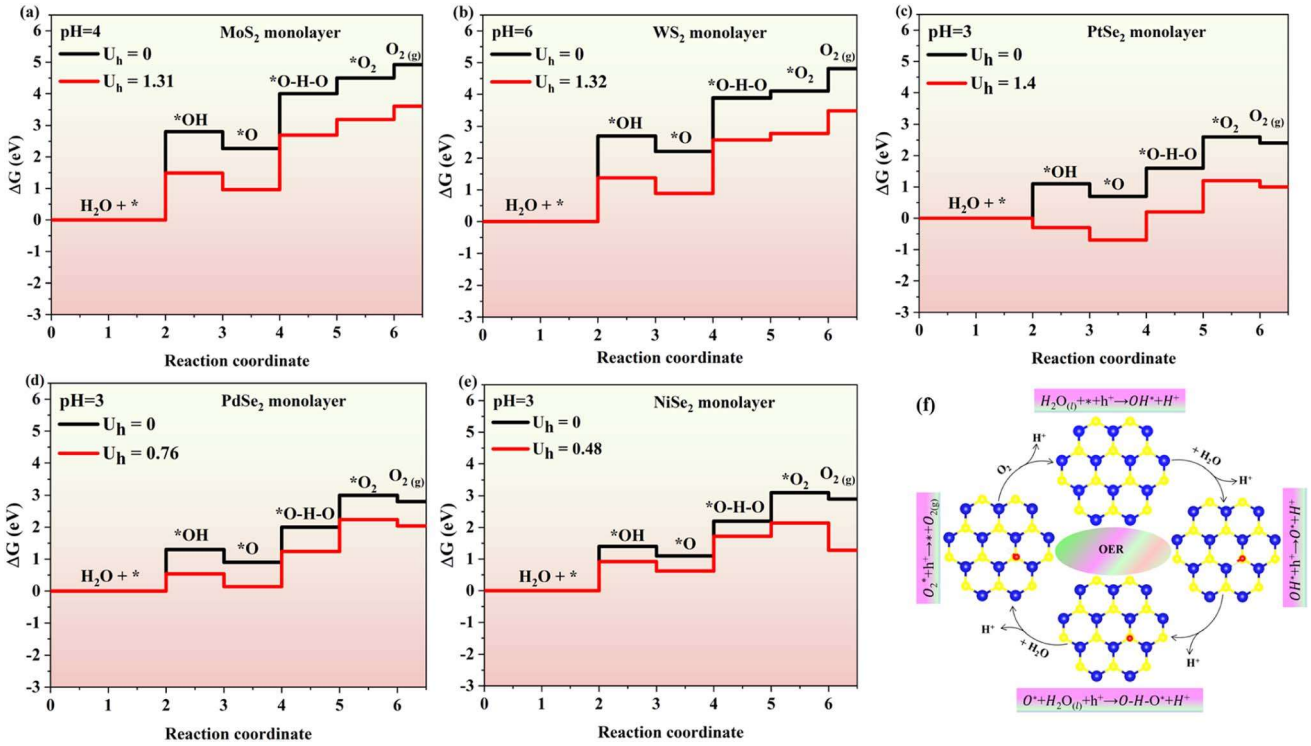

Fig. 3 (a–e) Gibbs free energy diagram for OER on MoS_2, WS_2, $PtSe_2$, $PdSe_2$ and $NiSe_2$ monolayers with energetically favourable absorbed intermediates (OH*, O*, O–H–O*, O_2^* and H*). (f) Schematic representation of the four-step OER process on the surface of MoS_2 monolayer.

$NiSe_2$ monolayers have ΔG (eV) values of HER near to zero. The more the ΔG (eV) value is near zero, the best is the photocatalyst for HER.[25,31,50,61,62] The overpotentials for HER on MoS_2, WS_2, $PtSe_2$, $PdSe_2$ and $NiSe_2$ monolayers are 0.43, 0.49, 0.19, 0.31 and 0.25 (unit, V), respectively. This observation underscores their potential as highly efficient catalysts for HER. A schematic representation of the two-step process of HER on the surface of the 2H-MoS_2 monolayer is shown in Fig. 4(c). The catalytic activity analysis shows that the predicted TMSS monolayers can function as a bi-functional photocatalyst towards OWS.

4.1 Solar to hydrogen (STH) conversion efficiency

We calculated the solar to hydrogen conversion efficiency (STH)[46] of the selected TMSS monolayers. According to the reaction process, STH efficiency (η_{STH}) is defined as the product of the efficiency of light absorption (η_{abs}) and carrier utilization (η_{cu}):

$$\eta_{STH} = \eta_{abs} \times \eta_{cu}. \tag{19}$$

The efficiency of light absorption is defined as follows:

$$\eta_{abs} = \frac{\int_{E_g}^{\infty} p(h\omega)\mathrm{d}(h\omega)}{\int_{0}^{\infty} p(h\omega)\mathrm{d}(h\omega)}, \tag{20}$$

where $p(h\omega)$ represents the solar energy flux at photon energy $h\omega$ for the AM1.5G spectrum and E_g represents the band gap of the photocatalyst. The denominator signifies the overall power density of the reference sunlight spectrum (AM1.5G), while the numerator quantifies the power density of the light absorbed by the photocatalyst. The efficiency of carrier utilization (η_{cu}) is defined as follows:

$$\eta_{cu} = \frac{\Delta G \int_{E}^{\infty} \frac{p(h\omega)}{h\omega}\mathrm{d}(h\omega)}{\int_{E_g}^{\infty} p(h\omega)\mathrm{d}(h\omega)}. \tag{21}$$

In this context, ΔG denotes the free energy associated with water splitting (1.23 eV), while the remaining terms in the numerator collectively quantify the effective photocurrent density. Additionally, E represents the photon energy utilized during the water splitting process, defined as follows:

$$E = \begin{cases} E_g, (\chi(H_2)) \geq 0.2,\ (\chi(O_2) \geq 0.6), \\ E_g + 0.2 - \chi(H_2), (\chi(H_2)) < 0.2, (\chi(O_2) \geq 0.6), \\ E_g + 0.6 - (\chi(O_2)), \chi(H_2) \geq 0.2, (\chi(O_2) < 0.6), \\ E_g + 0.8 - \chi(H_2) - \chi(O_2), (\chi(H_2)) < 0.2, (\chi(O_2) < 0.6). \end{cases}$$

The total energy conversion efficiency (η_{STH}), namely STH conversion efficiency, using the full solar spectrum is calculated as follows:

$$\eta_{STH} = \frac{\Delta G \int_{E}^{\infty} \frac{p(h\omega)}{h\omega}\mathrm{d}(h\omega)}{\int_{0}^{\infty} p(h\omega)\mathrm{d}(h\omega)}. \tag{22}$$

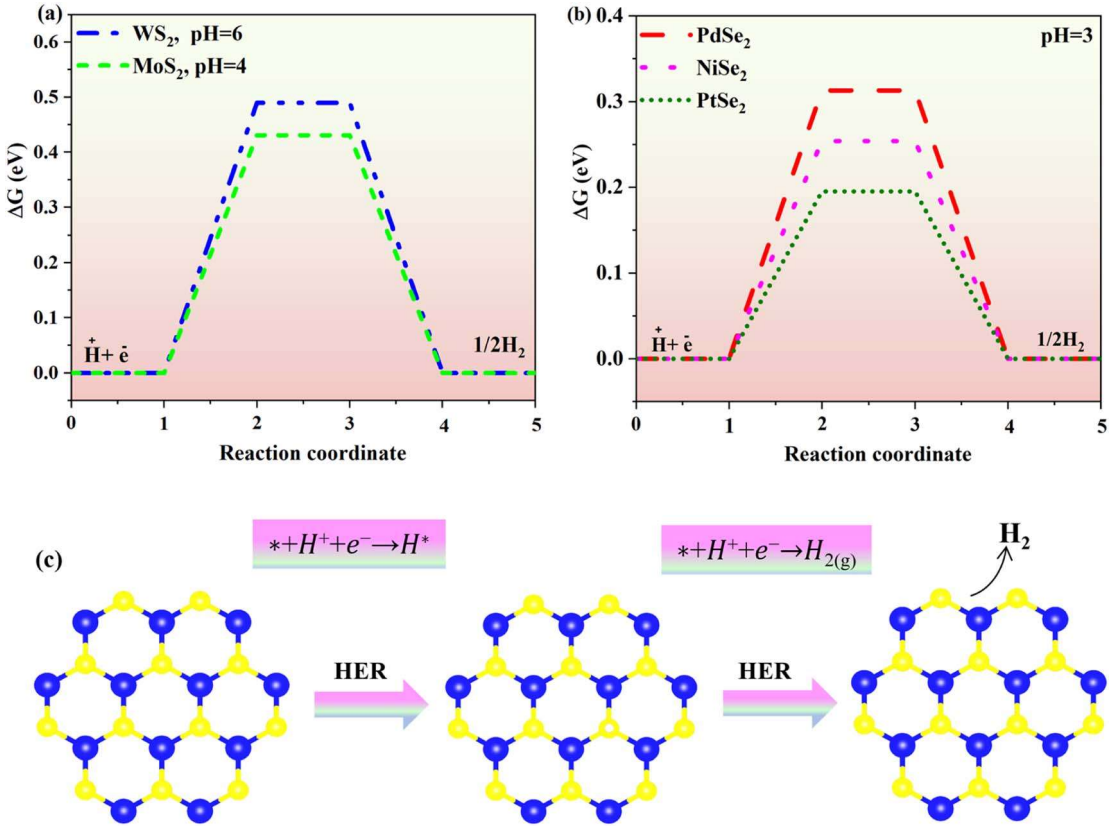

Fig. 4 Gibbs free energy diagram for HER on the surfaces of (a) MoS_2 and WS_2 monolayers, (b) $PdSe_2$, $PtSe_2$ and $NiSe_2$ monolayers with energetically favourable absorbed intermediates (OH*, O*, O–H–O*, O_2^* and H*) and (c) schematic representation of the two-step process of HER on the surface of 2H-MoS_2 monolayer.

For the pH effect, the calculated STH efficiencies are 10.4%, 11.1%, 22.2%, 19.6% and 20.9% for MoS_2, WS_2, $PtSe_2$, $PdSe_2$ and $NiSe_2$ monolayers, respectively. The predicted STH efficiencies exceed the required efficiency criterion (10%) of hydrogen conversion for commercial applications.[63] This is because the high STH efficiencies make the predicated TMSS monolayers outstanding candidates for hydrogen production. The calculated STH efficiencies for $MoSe_2$ and $SnSe_2$ monolayers in $MoSe_2/SnSe_2$ heterostructures are 10.5% and 9.3%, respectively, and for the pentagonal monolayer, $PdSe_2$ is 12.5%.[64,65] Similarly, the predicted STH efficiency for $MoSe_2$ monolayer in its heterojunction with Ti_2CO_2 is 12%.[66] The reported STH efficiencies for other TMSS monolayers align with our findings, confirming the promise of the selected materials. Remarkably, the predicted STH efficiencies for the monolayers surpass those reported in previous studies.

5. Conclusion

Transition metal sulfide and selenide (TMSS) monolayers were screened to find the best possible monolayers for overall water splitting. Properties such as suitable band edges, oxidation and reduction potentials, catalytic activities and solar to hydrogen (STH) efficiency were studied. Among various TMSS monolayers, MoS_2, WS_2, $PtSe_2$, $PdSe_2$, and $NiSe_2$ have suitable conduction and valence band edges to trigger the oxygen evolution reaction (OER) and hydrogen evolution reaction (HER) simultaneously in acidic media. Moreover, the MoS_2, $PtSe_2$, $PdSe_2$, and $NiSe_2$ monolayers can effectively resist oxidative and reductive photo-corrosion in acidic and WS_2 monolayer in neutral environments during water splitting. All monolayers have robust catalytic activities in the predicted electrolytes with HER overpotential near zero, and OERs are 0.53, 1.01 and 0.99 V for $PtSe_2$, $PdSe_2$ and $NiSe_2$ monolayers, respectively. The STH efficiencies were also found to be high for MoS_2 (10.4%), $PtSe_2$ (22.2%), $PdSe_2$ (19.6%), and $NiSe_2$ (20.1%) in acidic medium and WS_2 (11.1%) in neutral medium. The predicted monolayers show promise for practical applications as bifunctional photocatalysts in acidic and neutral environments.

Author contributions

Shafiq Ur Rehman: proposed idea, calculations, software, original draft. Junwei Wang: editing, reviewing. Guixuan Wu: editing, reviewing. Sajjad Ali: editing, reviewing. Jian Xian: Supervision, funding, editing, reviewing. Nasir Mahmood: Supervision, writing, editing, reviewing.

Conflicts of interest

All authors have declared no conflict of interest.

Acknowledgements

The present work was financially supported by the National Natural Science Foundation of China (No. 51972045 and 52202368), the Fundamental Research Funds for the Chinese Central Universities, China (No. ZYGX2019J025), Sichuan Science and Technology Program (No. 2021YFG0373). Thanks to prince sultan university for support. Special thanks to my wife and daughter (Sarah Shafiq) for their love and support throughout this work.

References

1 M. G. Walter, E. L. Warren, J. R. McKone, S. W. Boettcher, Q. Mi, E. A. Santori and N. S. Lewis, *Chem. Rev.*, 2010, **110**, 6446–6473.
2 A. Fujishima and K. J. N. Honda, *Nature*, 1972, **238**, 37–38.
3 P. Zhang, J. Zhang and J. Gong, *Chem. Soc. Rev.*, 2014, **43**, 4395–4422.
4 A. Kudo and Y. Miseki, *Chem. Soc. Rev.*, 2009, **38**, 253–278.
5 R. Li, Y. Weng, X. Zhou, X. Wang, Y. Mi, R. Chong, H. Han and C. Li, *Energy Environ. Sci.*, 2015, **8**, 2377–2382.
6 H. Lyu, T. Hisatomi, Y. Goto, M. Yoshida, T. Higashi, M. Katayama, T. Takata, T. Minegishi, H. Nishiyama and T. Yamada, *Chem. Sci.*, 2019, **10**, 3196–3201.
7 Y. Goto, T. Hisatomi, Q. Wang, T. Higashi, K. Ishikiriyama, T. Maeda, Y. Sakata, S. Okunaka, H. Tokudome and M. Katayama, *Joule*, 2018, **2**, 509–520.
8 T. Takata, J. Jiang, Y. Sakata, M. Nakabayashi, N. Shibata, V. Nandal, K. Seki, T. Hisatomi and K. Domen, *Nature*, 2020, **581**, 411–414.
9 Z. Zhao, R. V. Goncalves, S. K. Barman, E. J. Willard, E. Byle, R. Perry, Z. Wu, M. N. Huda, A. J. Moulé and F. E. Osterloh, *Energy Environ. Sci.*, 2019, **12**, 1385–1395.
10 X. Tao, Y. Zhao, S. Wang, C. Li and R. Li, *Chem. Soc. Rev.*, 2022, **51**, 3561–3608.
11 M. Melchionna and P. Fornasiero, *ACS Catal.*, 2020, **10**, 5493–5501.
12 M. Kumar, B. Meena, P. Subramanyam, D. Suryakala and C. Subrahmanyam, *NPG Asia Mater.*, 2022, **14**, 1–21.
13 R. Yang, Y. Fan, Y. Zhang, L. Mei, R. Zhu, J. Qin, J. Hu, Z. Chen, Y. Hau and D. Voiry, *Angew. Chem., Int. Ed.*, 2023, **62**, 18016–18029.
14 S. E. Jun, J. K. Lee and H. W. Jang, *Energy Adv.*, 2023, **2**, 34–53.
15 W. Zhang, K. Matsuda and Y. Miyauchi, *ACS Omega*, 2019, **4**, 10322–10327.
16 S. Chandrasekaran, L. Yao, L. Deng, C. Bowen, Y. Zhang, S. Chen, Z. Lin, F. Peng and P. Zhang, *Chem. Soc. Rev.*, 2019, **48**, 4178–4280.
17 T. Chowdhury, E. C. Sadler and T. J. Kempa, *Chem. Rev.*, 2020, **120**, 12563–12591.
18 S. Manzeli, D. Ovchinnikov, D. Pasquier, O. V. Yazyev and A. Kis, *Nat. Rev. Mater.*, 2017, **2**, 1–15.
19 Y. Xiao, C. Xiong, M. M. Chen, S. Wang, L. Fu and X. Zhang, *Chem. Soc. Rev.*, 2023, **52**, 1215–1272.
20 M. B. Wazir, M. Daud, S. Safeer, F. Almarzooqi and A. Qurashi, *ACS Omega*, 2022, **7**, 16856–16865.
21 Y. Sim, Y. Chae and S. Y. Kwon, *iScience*, 2022, **29**, 105098.
22 N. Karmodak and O. Andreussi, *ACS Energy Lett.*, 2020, **5**, 885–891.
23 Y. Wang, S. Zhao, Y. Wang, D. A. Laleyan, Y. Wu, B. Ouyang, P. Ou, J. Song and Z. Mi, *Nano Energy*, 2018, **51**, 54–60.
24 R. Lv, J. A. Robinson, R. E. Schaak, D. Sun, Y. Sun, T. E. Mallouk and M. Terrones, *Acc. Chem. Res.*, 2015, **48**, 56–64.
25 T. Rao, H. Wang, Y. J. Zeng, Z. Guo, H. Zhang and W. Liao, *Adv. Sci.*, 2021, **8**, 2002284.
26 Z. Shi, X. Zhang, X. Lin, G. Liu, C. Ling, S. Xi, B. Chen, Y. Ge, C. Tan and Z. Lai, *Nature*, 2023, **621**, 300–305.
27 Y. Zhao, Y. Chen, P. Ou and J. Song, *ACS Catal.*, 2023, **13**, 12941–12951.
28 Y. Chen, P. Ou, X. Bie and J. Song, *J. Mater. Chem. A*, 2020, **8**, 19522–19532.
29 M. Qorbani, A. Sabbah, Y. R. Lai, S. Kholimatussadiah, S. Quadir, C. Y. Huang, I. Shown, Y. F. Huang, M. Hayashi and K.-H. Chen, *Nat. Commun.*, 2022, **13**, 1256–1259.
30 J. D. Wiensch, J. John, J. M. Velazquez, D. A. Torelli, A. P. Pieterick, M. T. McDowell, K. Sun, X. Zhao, B. S. Brunschwig and N. S. Lewis, *ACS Energy Lett.*, 2017, **2**, 2234–2238.
31 X. Chia, A. Adriano, P. Lazar, Z. Sofer, J. Luxa and M. Pumera, *Adv. Funct. Mater.*, 2016, **26**, 4306–4318.
32 D. Saraf, S. Chakraborty, A. Kshirsagar and R. Ahuja, *Nano Energy*, 2018, **49**, 283–289.
33 G. Kresse and J. Furthmüller, *Phys. Rev. B: Condens. Matter Mater. Phys.*, 1996, **54**, 11169.
34 J. P. Perdew, K. Burke and M. Ernzerhof, *Phys. Rev. Lett.*, 1996, 77, 3865–3868.
35 H. J. Monkhorst and J. D. Pack, *Phys. Rev. B: Solid State*, 1976, **13**, 5188–5192.
36 S. Grimme, *J. Comput. Chem.*, 2004, **25**, 1463–1473.
37 K. Mathew, R. Sundararaman, K. L. Weaver, T. Arias and R. G. Hennig, *J. Chem. Phys.*, 2014, **140**, 084106–084108.
38 P. Giannozzi, S. Baroni, N. Bonini, M. Calandra, R. Car, C. Cavazzoni, D. Ceresoli, G. L. Chiarotti, M. Cococcioni and I. Dabo, *J. Phys.: Condens.Matter*, 2009, **21**, 395502–395509.
39 A. Togo, F. Oba and I. Tanaka, *Phys. Rev. B: Condens. Matter Mater. Phys.*, 2008, **78**, 134106.
40 R. Dong, A. Jacob, S. Bourdais and S. Sanvito, *npj 2D Mater. Appl.*, 2021, **5**, 26–35.
41 S. Haastrup, M. Strange, M. Pandey, T. Deilmann, P. S. Schmidt, N. F. Hinsche, M. N. Gjerding, D. Torelli, P. M. Larsen and A. C. Riis-Jensen, *2D Mater.*, 2018, **5**, 042002–042009.
42 F. A. Rasmussen and K. S. Thygesen, *J. Phys. Chem. C*, 2015, **119**, 13169–13183.
43 J. Zhou, L. Shen, M. D. Costa, K. A. Persson, S. P. Ong, P. Huck, Y. Lu, X. Ma, Y. Chen and H. Tang, *Sci. Data*, 2019, **6**, 86–90.
44 A. Mishra, S. Satsangi, A. C. Rajan, H. Mizuseki, K. R. Lee and A. K. Singh, *J. Phys. Chem. Lett.*, 2019, **10**, 780–785.
45 L. Ju, J. Shang, X. Tang and L. Kou, *J. Am. Chem. Soc.*, 2019, **142**, 1492–1500.

46 C. F. Fu, J. Sun, Q. Luo, X. Li, W. Hu and J. Yang, *Nano Lett.*, 2018, **18**, 6312–6317.
47 Y. Jing, Z. Zhou, W. Geng, X. Zhu and T. Heine, *Adv. Mater.*, 2021, **33**, 2008645–2008648.
48 T. Yu, C. Wang, X. Yan, G. Yang and U. Schwingenschlogl, *J. Phys. Chem. Lett.*, 2021, **12**, 2464–2470.
49 R. da Silva, R. Barbosa, R. R. Mancano, N. Duraes, R. B. Pontes, R. Miwa, A. Fazzio and J. E. Padilha, *ACS Appl. Nano Mater.*, 2019, **2**, 890–897.
50 S. Hussain, K. Akbar, D. Vikraman, I. Rabani, W. Song, K. S. An, H. S. Kim, S. H. Chun and J. Jung, *J. Mater. Res. Technol.*, 2021, **12**, 385–398.
51 A. Mondal and A. Vomiero, *Adv. Funct. Mater.*, 2022, **32**, 2208994.
52 S. Chen and L. W. Wang, *Chem. Mater.*, 2012, **24**, 3659–3666.
53 C. Jian, W. Hong, Q. Cai, J. Li and W. Liu, *Appl. Catal., B*, 2020, **266**, 118649.
54 J. Zhang, T. Wang, P. Liu, S. Liu, R. Dong, X. Zhuang, M. Chen and X. Feng, *Energy Environ. Sci.*, 2016, **9**, 2789–2793.
55 J. Liang, Y. Wang, Q. Liu, Y. Luo, T. Li, H. Zhao, S. Lu, F. Zhang, A. M. Asiri and F. Liu, *J. Mater. Chem. A*, 2021, **9**, 6117–6122.
56 Y. Ge, S. P. Gao, P. Dong, R. Baines, P. M. Ajayan, M. Ye and J. Shen, *Nanoscale*, 2017, **9**, 5538–5544.
57 P. Thangasamy, V. Maruthapandian, V. Saraswathy and M. Sathish, *Catal. Sci. Technol.*, 2017, **7**, 3591–3597.
58 Y. Zhao, J. Hwang, M. T. Tang, H. Chun, X. Wang, H. Zhao, K. Chan, B. Han, P. Gao and H. Li, *J. Power Sources*, 2020, **456**, 227998–227999.
59 S. Chen, T. Takata and K. Domen, *Nat. Rev. Mater.*, 2017, **2**, 1–17.
60 J. K. Nørskov, J. Rossmeisl, A. Logadottir, L. Lindqvist, J. R. Kitchin, T. Bligaard and H. Jonsson, *J. Phys. Chem. B*, 2004, **108**, 17886–17892.
61 C. S. Gopinath and N. Nalajala, *J. Mater. Chem. A*, 2021, **9**, 1353–1371.
62 D. Voiry, R. Fullon, J. Yang, C. de C. Castro e Silva, R. Kappera, I. Bozkurt, D. Kaplan, M. J. Lagos, P. E. Batson, G. Gupta, A. D. Mohite, L. Dong, D. Er, V. B. Shenoy, T. Asefa and M. Chhowalla, *Nature*, 2016, **15**, 1003–1009.
63 C. R. Cox, J. Z. Lee, D. G. Nocera and T. Buonassisi, *Proc. Natl. Acad. Sci. U. S. A.*, 2014, **111**, 14057–14061.
64 Y. Fan, J. Wang and M. Zhao, *Nanoscale*, 2019, **11**, 14836–14843.
65 C. Long, Y. Liang, H. Jin, B. Huang and Y. Dai, *ACS Appl. Energy Mater.*, 2018, **2**, 513–520.
66 C. F. Fu, X. Li and J. Yang, *Chem. Sci.*, 2021, **12**, 2863–2869.

